J. Meas. Sci. Instrum., 2025, 16(3): 323-333. http://jmsi.publish.founderss.cn/
DOI: 10.62756/jmsi.1674-8042.2025031 jmsi@nuc.edu.cn

Design of phononic crystal plate with folded helical beam for vibration isolation in MEMS resonators

LI Siyi, XU Lijiang, JIANG Bo*

School of Mechanical Engineering, Nanjing University of Science and Technology, Nanjing 210094, China

***Corresponding author:** JIANG Bo (bjiang@njust.edu.cn)

Received: June 27, 2025 **Revised:** August 24, 2025 **Accepted:** September 1, 2025

Abstract: Enhancing the vibration resistance of micro-electro-mechanical systems (MEMS) resonators in complex environments is a critical issue that urgently needs to be addressed. This paper presents a chip-scale locally resonant phononic crystal (LRPnC) plate based on a folded helical beam structure. Through finite element simulation and theoretical analysis, the bandgap characteristics and vibration suppression mechanisms of this structure were thoroughly investigated. The results show that the structure exhibits a complete bandgap in the frequency range of 9.867—14.605 kHz, and the bandgap can be effectively tuned by adjusting the structural parameters. Based on this, the influence of the number of unit cell layers on the vibration reduction performance was further studied, and a finite periodic LRPnC plate was constructed. Numerical studies have shown that the LRPnC plate can achieve more than -30 dB of vibration attenuation within the bandgap and effectively suppress y-direction coupling vibrations caused by x-direction propagating waves. In addition, its chip-scale size and planar structure design provide new ideas and methods for the engineering application of phononic crystal technology in the field of MEMS vibration isolation.

Key words: micro-electro-mechanical systems (MEMS) resonators; vibration isolation; locally resonant phononic crystals (LRPnC); chip-level acoustic metamaterials; finite element simulation

0 Introduction

Micro-electro-mechanical systems (MEMS) resonators, with their advantages of miniaturization, low power consumption, and batch manufacturability, have become the core components of modern inertial sensing, communication, and precision measurement systems[1-3]. With the continuous development of micro- and nano-fabrication technologies, the applications of MEMS resonators in consumer electronics, aerospace navigation, and national defense security are becoming increasingly widespread[4-6]. However, mechanical vibration interferences in complex environments can cause frequency drift and a decrease in the quality factor (Q value) of the resonators, thereby severely limiting their performance enhancement[7,8].

Phononic crystals (PnCs), as a novel type of artificial periodic material, offer an innovative solution for vibration isolation with their unique elastic wave bandgap characteristics[9]. By forming elastic wave stopbands within specific frequency ranges, PnCs can effectively suppress vibrations in the target frequency bands. Depending on the bandgap formation mechanisms, PnCs are mainly divided into two categories: traditional PnCs based on Bragg scattering[10] and PnCs based on local resonance[11]. Among them, locally resonant phononic crystals (LRPnCs) exhibit excellent low-frequency bandgap characteristics and can effectively control long-wavelength vibrations in small-sized structures, which gives them unique advantages in vibration isolation designs for MEMS devices[12].

In recent years, significant progress has been made in the research of LRPnCs. Yao et al.[13] achieved an impressive 30 dB attenuation in the target frequency band through the design of 3D phononic crystal metamaterials and verified its excellent compatibility with standard MEMS manufacturing processes. The Zega team[14] proposed a defect-based MEMS phononic crystal waveguide, which achieved precise control of the propagation path of elastic waves and effectively solved the problem of excessive anchor loss in traditional MEMS resonators. Chai et al.[15] designed a gradient spiral beam structure that leverages the rainbow trapping

effect to achieve an average attenuation of 35 dB in the low-frequency bands of 50.5 — 100.1 Hz and 119.8 — 165.8 Hz, highlighting the unique advantages of LRPnCs in low-frequency vibration control. Despite significant breakthroughs in theoretical research and technological implementation, the size of existing phononic crystal structures still severely restricts their application in low-frequency vibration isolation for MEMS resonators, especially for MEMS gyroscopes operating in the 10—20 kHz frequency band, where this issue is particularly pronounced.

To address these challenges, this study proposes a chip-scale LRPnC plate structure based on a folded helical-beam design. Finite element simulation validation indicates that the structure can achieve stable attenuation exceeding —30 dB under z-direction displacement excitation within the bandgap frequency range of 9.867—14.605 kHz, while effectively suppressing y-direction vibrations induced by the lattice coupling effect from x-direction propagating elastic waves. This research aims to enhance the vibration resistance of MEMS resonators in complex vibration environments and to provide new ideas and methods for the design of high-performance MEMS devices.

1 Analysis of folded helical beam LRPnC

1.1 Unit cell model and band structure of folded helical beam LRPnC

1.1.1 Unit cell model of LRPnC based on folded helical beam structure

This study proposes a novel chip-scale LRPnC plate structure to meet the vibration suppression requirements of MEMS resonators operating in the 10—20 kHz frequency band. The structure is composed of periodically arranged folded helical beam LRPnC unit cells, as show in Fig.1. The unit cell is made of single-crystal silicon and consists of an external frame, four sets of folded helical beams, and a central mass block, forming an integrated structure. The planar design of this structure is fully compatible with MEMS fabrication processes. After systematic parametric simulation optimization and considering the performance requirements for the target operating frequency band (10—20 kHz) as well as the manufacturing limitations of the silicon on insulator (SOI) micro- and nano-fabrication process, we finally determined the optimal geometric parameters of the phononic crystal structure, including lattice constant a, frame width b, beam width c, side length of central mass block d, and thickness H. The specific values are detailed in Table 1. Meanwhile, single-crystal silicon, as the core material for MEMS devices, has the characteristics of high strength, high hardness, corrosion resistance, ease of processing, and compatibility with IC processes. The specific material parameters are listed in Table 2.

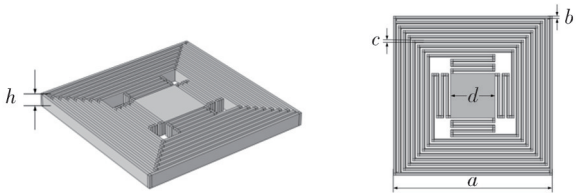

(a) Schematic diagram of unit cell (b) Top view of unit cell

Fig. 1 Phononic crystal structure

Table 1 Dimensional parameters of unit cell

Parameter	Value
Lattice constant a/μm	400
Frame width b/μm	6
Width of folded helical beam c/μm	6
Side length of central mass block d/μm	112
Thickness h/μm	30

Table 2 Properties of silicon material

Parameter	Value
Density ρ/(kg•m^{-3})	2 330
Young's modulus E/GPa	169
Poisson's ratio ν	0.28

1.1.2 Calculation of band structure

The band structure of phononic crystals can intuitively reflect the main characteristics of bandgaps, such as the starting and ending frequencies and the width of the bandgap. It is the primary basis for studying phononic crystal structures and one of the main criteria for determining the application scenarios of phononic crystal structures[16]. Based on Bloch's theory, the periodic nature of phononic crystals allows the study of their vibrational characteristics to be simplified to the analysis of a single unit cell. Specifically, by applying periodic boundary conditions at the boundaries of a single unit cell and introducing the Bloch wave vector $\boldsymbol{k}$, the eigen-vibration characteristics of an infinitely periodic phononic crystal structure can be obtained by solving the characteristic equation as $\boldsymbol{k}$ varies along the irreducible Brillouin zone boundary[17]. This method provides the theoretical foundation for the calculation of the band structure.

In this study, the finite element simulation software is used to set the components k_x and k_y of the wave vector along the irreducible Brillouin zone M-Γ-X-M (Fig.2(a)) as

$$k_x=\begin{cases}\dfrac{\pi}{a}(1-m), & 0\leqslant m\leqslant 1,\\ \dfrac{\pi}{a}(m-1), & 1<m\leqslant 2,\\ \dfrac{\pi}{a}, & 2<m\leqslant 3,\end{cases} \tag{1}$$

$$k_y=\begin{cases}\dfrac{\pi}{a}(1-m), & 0\leqslant m\leqslant 1,\\ 0, & 1<m\leqslant 2,\\ \dfrac{\pi}{a}(m-2), & 2<m\leqslant 3,\end{cases} \tag{2}$$

where m is a scanning parameter.

As shown in Fig.2 (b), the calculated band structure of the phononic crystal exhibits a significant complete bandgap in the frequency range of 9.867 — 14.605 kHz, with a bandgap width of 4.738 kHz. Under the ideal condition of an infinite periodic array, this complete bandgap can achieve omnidirectional (in the x-, y-, and z-directions) suppression of elastic waves, offering superior applicability compared to traditional directional bandgaps. This bandgap range precisely covers the low-frequency region (10 — 14.605 kHz) of the 10—20 kHz operating frequency band of MEMS resonators, effectively suppressing harmful vibrations within this frequency range and meeting the design requirements. Additionally, due to the flatness of the band structure, multiple directional bandgaps are also observed in other frequency ranges, which can effectively suppress the propagation of vibrations in specific directions[18].

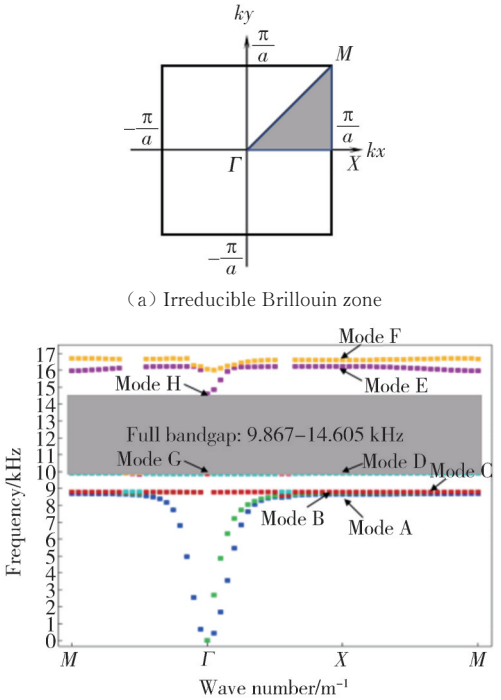

(a) Irreducible Brillouin zone

(b) Band structure of folded helical beam LRPnC

Fig. 2 Irreducible Brillouin zone and band structure

1.2 Vibration model and bandgap characteristic analysis of LRPnC

Investigating the bandgap formation mechanisms is a necessary prerequisite for developing novel phononic crystal structures. To gain an in-depth understanding of the local resonance modes of the folded helical beam LRPnC and the mechanisms behind its bandgap generation, we selected characteristic points A to H from the band diagram and plotted the corresponding vibration modes at the flat bands and cutoff frequencies for each frequency band, as shown in Fig.3 (a) —3 (h).

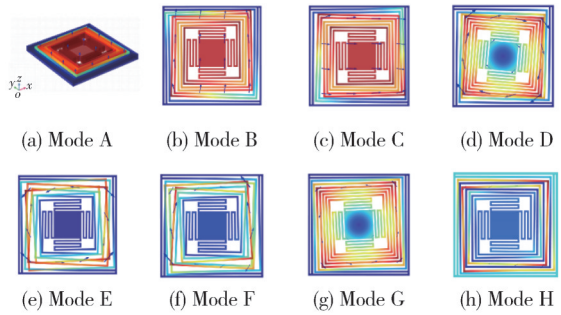

(a) Mode A (b) Mode B (c) Mode C (d) Mode D

(e) Mode E (f) Mode F (g) Mode G (h) Mode H

Fig. 3 Local resonance modes of unit cell

Modes A—F correspond to the vibration modes of the flat band regions of each frequency band, indicating that the unit cell exhibits almost identical natural frequencies in all directions. This characteristic is due to the high symmetry of the structure. Modes G and H represent the critical vibration modes corresponding to the lower edge of the bandgap (9.867 kHz) and the upper edge of the bandgap (14.605 kHz), respectively.

From these modes, it can be seen that except for mode H, where both the external frame and the internal structure vibrate, the other modes all have the external frame remaining stationary, with displacements mainly concentrated in the central mass block and the folded helical beams. For instance, mode A corresponds to the vibration mode of the central mass block and the folded helical beams perpendicular to the plate direction, while modes B—G correspond to their longitudinal, transverse, and torsional vibrations within the plane. This type of localized resonance is referred to as a "local resonance mode". Here, the central mass block and the four sets of folded helical beams form an "internal resonant unit", which absorbs external vibration energy through resonance with external vibrations, thereby effectively suppressing the propagation of elastic waves.

Due to the rotational symmetry of the unit cell, it can be equivalently modeled as the "mass-spring-frame" model shown in Fig. 4 under the aforementioned vibration modes[19]. Its natural frequencies are determined by its equivalent mass and equivalent stiffness and can be expressed as[20]

$$f=\frac{\omega}{2\pi}=\frac{1}{2\pi}\sqrt{\frac{k_e}{m_e}}, \tag{3}$$

where m_e represents the equivalent mass, and k_e

represents the equivalent stiffness. For different resonance modes, the equivalent mass and equivalent stiffness also differ. Therefore, by optimizing the structural geometric parameters (such as beam width, size of the central mass block, etc.), precise control of the equivalent mass and equivalent stiffness can be achieved, enabling active design of the bandgap frequency range.

Theoretical analysis based on the "mass-spring-frame" model indicates that when the excitation frequency of the external elastic wave approaches the natural frequency of the internal resonant unit within the phononic crystal, significant local resonance occurs in the system. At the same time, the internal resonant unit exerts a reaction force on the external frame, as shown in Fig. 4. When the force generated by the elastic wave is equal in magnitude to the reaction force produced by the internal resonant unit, the vibration energy tends to zero due to the cancellation of the two forces, thereby forming a bandgap.

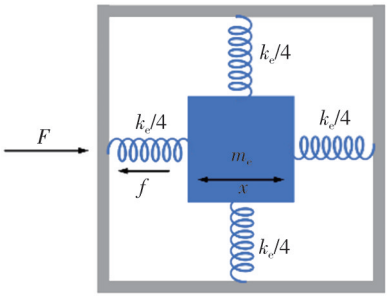

Fig. 4 Equivalent "mass-spring-frame" model of unit cell

2 Vibration transmission characteristics of finite-period LRPnC

2.1 Calculation of transmission characteristics curve

The band structure calculation can provide the bandgap frequency and width for an infinitely periodic phononic crystal. However, in practical engineering applications, only finite-sized phononic crystal structures can be designed. Therefore, to quantify the attenuation of elastic waves by a finite-sized phononic crystal structure, it is necessary to calculate the energy transmission spectrum of the finite structure, namely the transmission characteristics curve[21].

Taking the phononic crystal structure studied in this paper as an example, the process of calculating the transmission characteristics curve is introduced as follows.

Firstly, construct the geometric model of the phononic crystal in the finite element simulation software (assuming it is composed of a 3×3 arrangement of unit cells), as shown in Fig. 5. Next, mesh the model and accurately define the material parameters. After that, select the solid mechanics physics field, apply a displacement excitation with an amplitude of μ_0 on the left boundary to simulate the incident elastic wave, and set the right boundary as a free boundary condition. Finally, input the target frequency range in the solver settings and perform the frequency-domain solution calculation. After the solution is completed, we obtain the displacement response values at the input and output boundaries of the phononic crystal through post-processing, and then calculate the vibration energy attenuation rate T according to the formula as

$$T = 20 \lg \frac{|d_{\text{out}}|}{|d_{\text{in}}|}, \tag{4}$$

where d_{out} represents the output displacement value, and d_{in} represents the input displacement value.

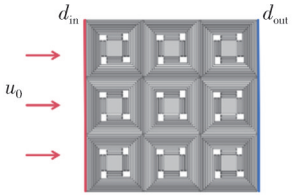

Fig. 5 Finite element model for calculating transmission characteristics curve

Based on this formula, with frequency f as the horizontal axis and energy transmission rate T as the vertical axis, the transmission characteristics curve of the finite-period phononic crystal structure can be obtained.

2.2 Influence of different cell layers on vibration attenuation characteristics

In silicon phononic crystal thin plate structures, the propagation of elastic waves is primarily dominated by the A0 mode of Lamb waves[22]. Therefore, we used z-direction displacement excitation to activate the main wave mode and collected the corresponding displacement response[23]. By employing the method for calculating the transmission characteristics curve, we quantitatively analyzed the attenuation characteristics of vibration energy during its propagation.

Given that elastic waves mainly propagate along the x-direction in thin plates and that the periodic arrangement in the y-direction has a minimal impact on the bandgap characteristics [24], we focused on studying the influence of the 1—6 layer unit cell arrays in the x-direction on the

vibration transmission characteristics. First, we established a finite element model of a phononic crystal with six periodic structures using finite element simulation software, as shown in Fig.6 (a).

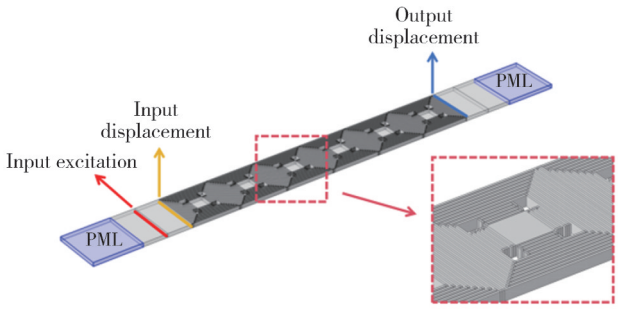

(a) Simulation for transmission curve of a 6-layer unit cell structure

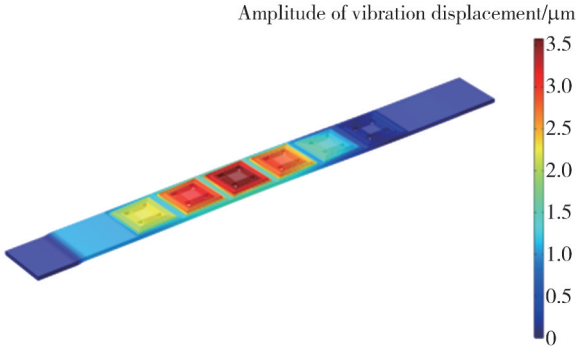

(b) Frequency response mode at 6.25 kHz

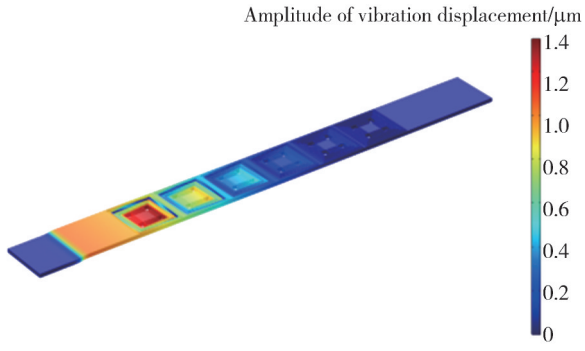

(c) Frequency response mode at 12 kHz

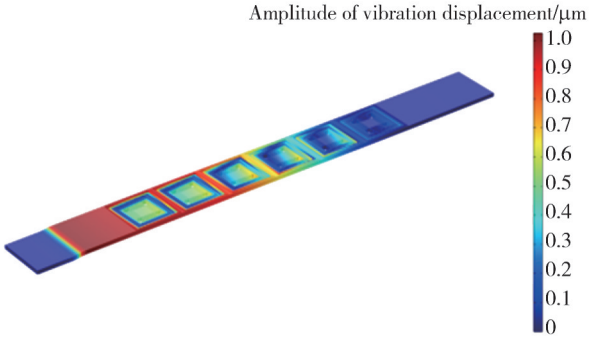

(d) Frequency response mode at 18 kHz

Fig. 6 Simulation and frequency response modes of phononic crystal structure

A z-direction displacement excitation with an amplitude of 1 μm was applied to the left side of the model to excite elastic waves. Displacement input and output detection surfaces were set on both sides of the structure, and a perfectly matched layer (PML) was configured to eliminate the influence of boundary reflections on the simulation results[25].

The frequency response of the phononic crystal is shown in Fig.6 (b)—(d). The simulation results indicate that under excitation frequencies outside the bandgap (6.25 kHz and 18 kHz), the elastic acoustic waves have propagated to the sixth unit cell. However, when excited at the bandgap frequency (12 kHz), the elastic wave is almost completely absorbed by the third unit cell position during propagation and cannot continue to propagate further.

To further investigate the impact of varying phononic crystal layer counts on transmission characteristics, numerical simulations were conducted on structures comprising 1 to 6 layers of unit cells. Fig.7 (a) presents the vibration transmission curves corresponding to these different layer configurations. Under z-direction excitation, the system predominantly activates mode A, as described in sections 1.2, with energy dissipation primarily occurring through the longitudinal vibration of the unit cells along the excitation axis.

The research findings reveal that within the bandgap frequency range of 9.867—14.605 kHz (indicated by the light gray area in the figure), when the number of unit cell layers is 1—3, the attenuation values within the bandgap frequencies remain below 20 dB, failing to meet effective vibration isolation requirements. However, when the layer count increases to 4, the attenuation amplitude significantly improves to over 40 dB, indicating that the structure has achieved satisfactory vibration isolation performance. Notably, further increasing the unit cell layers to 5 and 6 does not yield substantial improvement in attenuation effectiveness.

To further validate this phenomenon, Fig.7 (b) — (g) present the frequency response modes of 1—6 layer unit cell arrays at 12 kHz (near the center frequency of the bandgap). It can be clearly observed that the output end of the unit cell arrays in layers 1 to 3 still exhibits significant displacement responses, whereas the displacement at the output end of the unit cell arrays in layers 4 to 6 has essentially vanished, indicating that the elastic waves have been effectively suppressed. In addition, near 8.8 kHz outside the bandgap, abnormal attenuation phenomena were observed in the 1—6 layer unit cells. This phenomenon may originate from the strong local resonance effect of the first unit cell, resulting in the absorption of a large amount of vibrational energy.

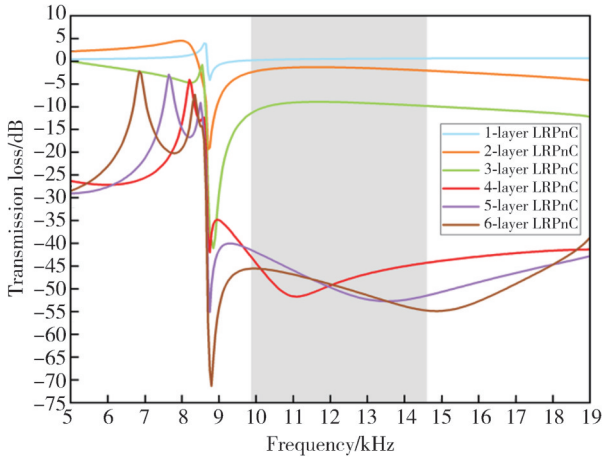

(a) Transmission characteristics curves for unit cell structures with different number of layers (1–6 layers)

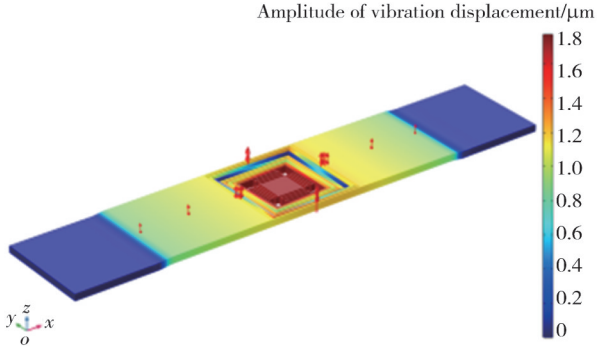

(b) 1-layer unit cell structure at 12 kHz

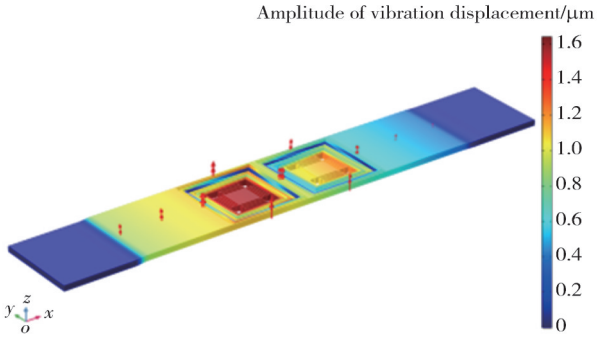

(c) 2-layer unit cell structure at 12 kHz

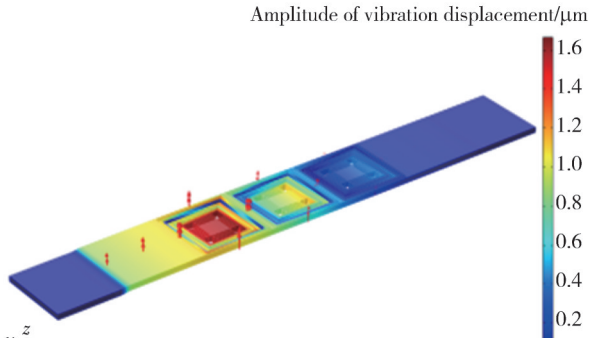

(d) 3-layer unit cell structure at 12 kHz

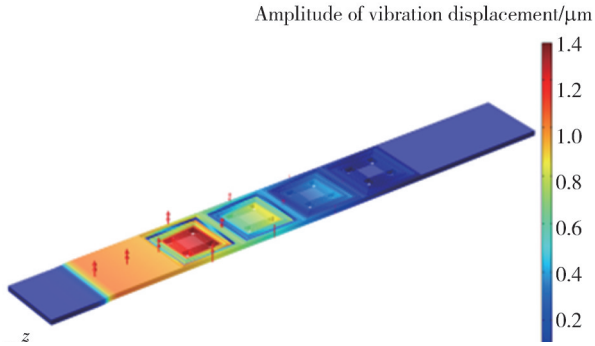

(e) 4-layer unit cell structure at 12 kHz

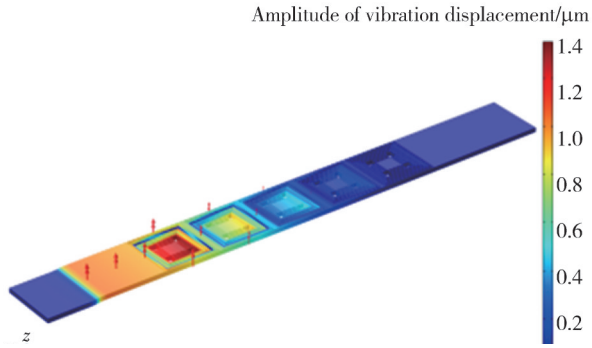

(f) 5-layer unit cell structure at 12 kHz

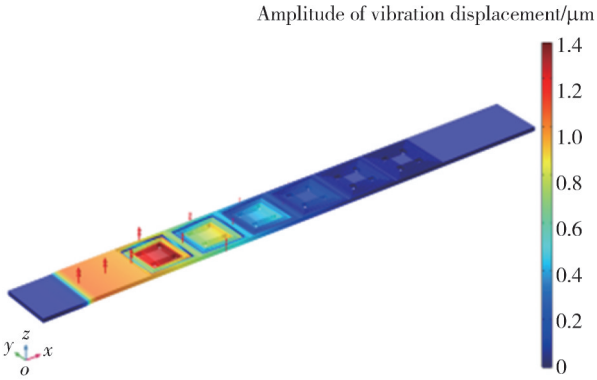

(g) 6-layer unit cell structure at 12 kHz

Fig. 7 Transmission characteristics and frequency response modes for unit cell structures with different layer numbers

Based on the above analysis, since the four-layer unit cell structure has already met the vibration attenuation requirements, we focused on analyzing its vibration attenuation characteristics and plotted the transmission characteristic curves of the structure in the x-, y-, and z-directions, as shown in Fig.8(a).

The simulation results indicate that within the band-gap frequency range of 9.867—14.605 kHz, the elastic wave exhibits the expected significant attenuation in the excitation direction (z-direction), with a peak attenuation value of —57.71 dB, demonstrating excellent vibration-isolation performance of the structure in the z-direction. It is worth noting that significant vibration attenuation is also observed in the non-excited y-direction, with a maximum attenuation value of —37.57 dB. This result suggests that the phononic crystal structure also has a significant suppression effect on the coupled vibration components in the y-direction. However, for the coupled components in the x-direction, the structure does not exhibit a noticeable suppression effect.

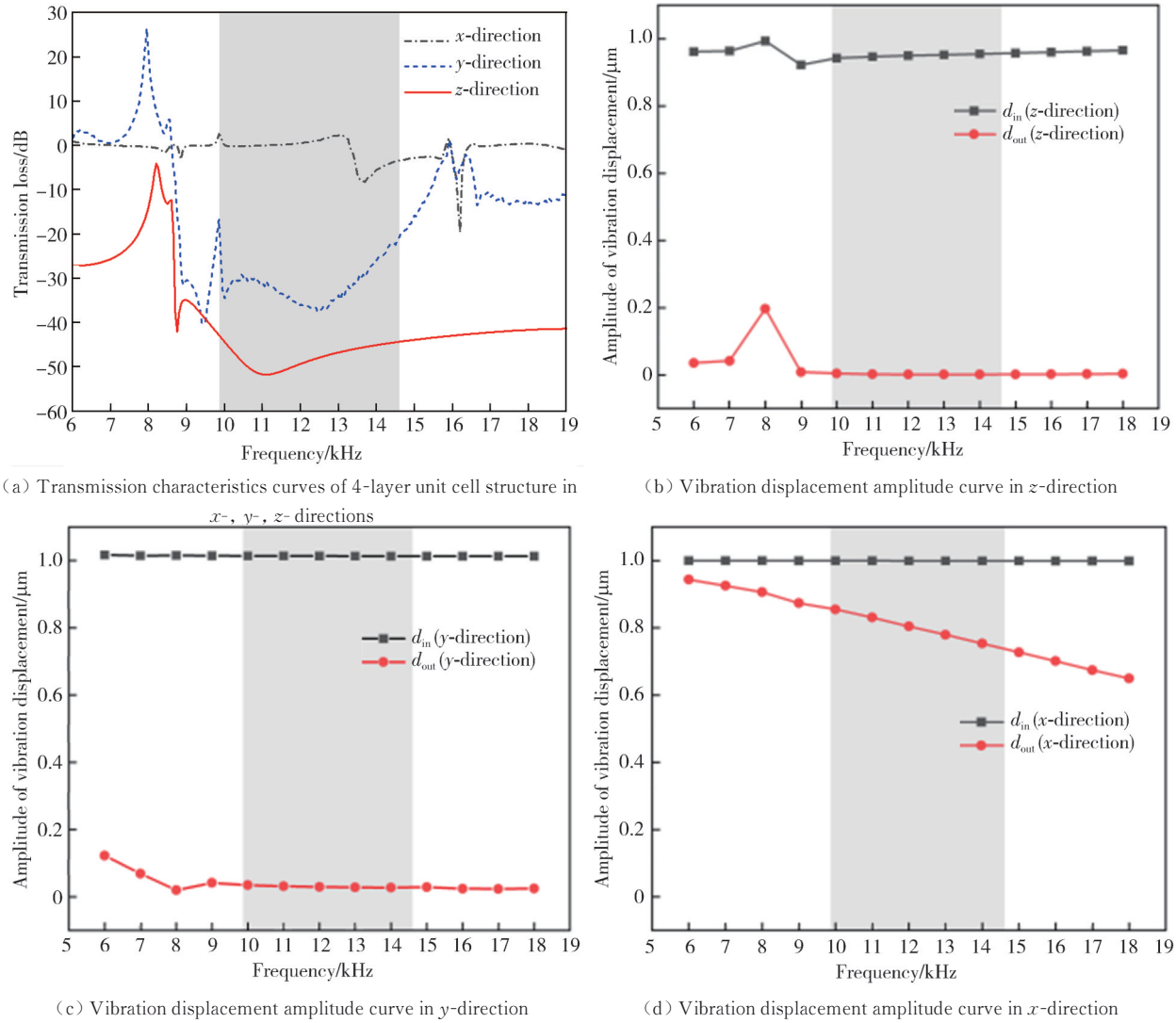

(a) Transmission characteristics curves of 4-layer unit cell structure in x-, y-, z- directions

(b) Vibration displacement amplitude curve in z-direction

(c) Vibration displacement amplitude curve in y-direction

(d) Vibration displacement amplitude curve in x-direction

Fig. 8 Transmission characteristic curves and vibration displacement amplitude curves of fourth-layer unit cell structure

To further verify its attenuation characteristics for the coupled components in the y-direction and the relatively weaker attenuation features in the x-direction, we conducted a quantitative analysis. First, we plotted the average displacement amplitude curves of the input and output detection surfaces when the structure was excited in the z-direction, as shown in Fig. 8(b). Meanwhile, we applied the same displacement excitation of 1 μm in both the x- and y-directions and plotted the corresponding vibration displacement amplitude curves, as shown in Fig. 8(c) and (d). The results clearly show that within the band-gap frequency range, when the input detection average displacement is approximately 1 μm, the output displacement detection average values in the y- and z-directions are almost 0, while the maximum attenuation displacement in the x-direction is only reduced by about 0.27 μm.

Further analysis reveals that the actual effective attenuation bandwidths in both the y-direction and z-direction exceed the theoretical bandgap width. This is attributed to the existence of multiple modes of Lamb waves propagating in silicon phononic crystals, where different modes of Lamb waves are excited with varying degrees of difficulty under the same excitation conditions[26]. In this study, we focus on the propagation characteristics of Lamb

waves in thin silicon plate structures, with particular emphasis on the A0 mode of Lamb wave propagation. The propagation characteristics of this specific mode lead to the observed phenomenon of the actual attenuation bandwidth being greater than the theoretical bandgap width.

The above findings reveal a key characteristic of the structure: when an excitation is applied in the z-direction, the elastic wave propagating along the x-direction can further excite the vibration components in the y-direction through the lattice coupling effect and significantly suppress them. This indicates that the energy transfer of elastic waves between different directions is not entirely independent but can be coupled through the interaction of the lattice. Moreover, the designed phononic crystal not only breaks through the limitations of traditional unidirectional attenuation but also achieves coordinated suppression of vibrations in multiple directions. This characteristic endows it with higher value in engineering applications, especially in complex scenarios where vibrations in multiple directions need to be controlled simultaneously.

2.3 Vibration damping characteristics of LRPnC plate and potential application scenarios

Based on the aforementioned research on the vibration transmission characteristics of the folded helical beam LRPnC, we have designed a novel LRPnC plate to enhance its engineering applicability for vibration attenuation. The plate consists of 16 unit cells arranged in a 4×4 periodic array, as illustrated in Fig.9(a) and (b). Individual unit cells are interconnected via an external framework. This connection allows for the transfer of vibrational energy between the unit cells but does not significantly alter the internal vibration characteristics of each cell.

As analyzed in Section 1.2 for the vibration model of the LRPnC, the resonance frequency of this locally resonant phononic crystal structure is primarily determined by the internal central mass block and the folded spiral beam. Under the "local resonance mode", the external framework remains stationary, and the vibrational energy is mainly concentrated in the internal structure. Therefore, even when the unit cell array is expanded to a 4×4 configuration, as long as the geometric dimensions and material properties of the central mass block and folded spiral beam within each unit cell remain unchanged, the resonance frequency will not be significantly affected.

To effectively absorb the vibrational energy at the boundaries, PML layers are also set on both sides of the plate as absorbing boundary conditions.

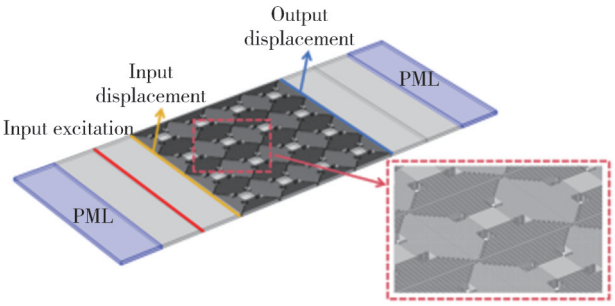

(a) Simulation for transmission curve of LRPnC plate

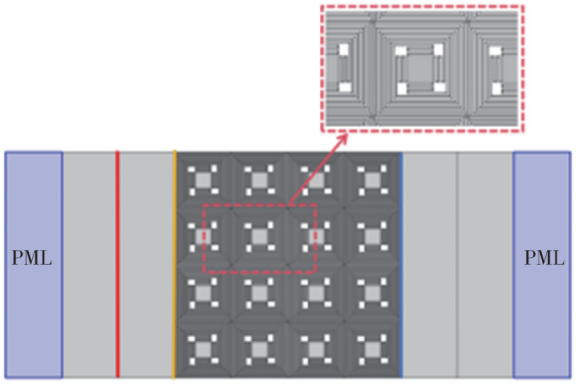

(b) Top view of LRPnC plate

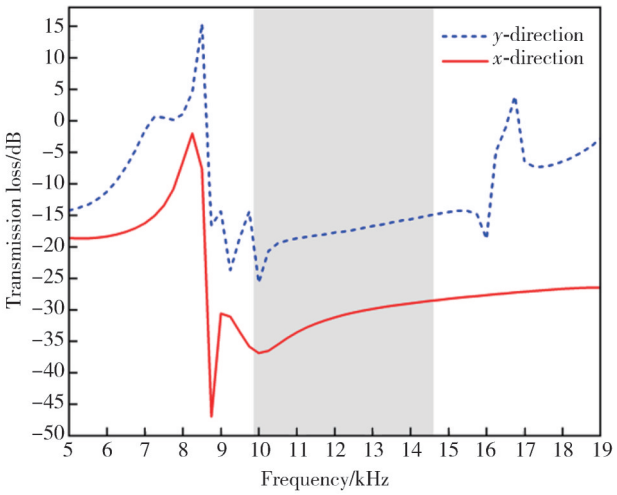

(c) Transmission characteristics curves of LRPnC plate in y- and z- directions

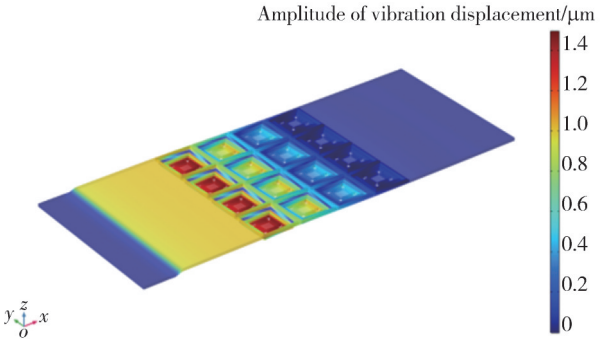

(d) Frequency response mode of LRPnC plate at 12 kHz

Fig. 9 Simulation and transmission characteristics of LRPnC plate

Using the same finite element method as previously described, we analyzed the vibration transmission characteristics of this structure, with the vibration transmission characteristic curve shown in Fig.9(c). The frequency response mode of the LRPnC plate under a 12 kHz frequency excitation is depicted in Fig.9(d).

The finite element simulation results reveal the outstanding vibration suppression capability of the structure within the bandgap frequency range (9.867—14.605 kHz), as detailed below:

1) Vibration attenuation in z-direction

In the excitation direction along the z-direction, the structure achieves stable attenuation of −30 dB and below, with a maximum attenuation amplitude reaching −36.75 dB. The effective attenuation bandwidth (attenuation >20 dB) is significantly wider than the bandgap width, demonstrating excellent broadband vibration suppression performance. In contrast, traditional unidirectional vibration-damping structures typically achieve significant attenuation only at specific frequency points, with limited effectiveness across a broad frequency band.

2) Coupled vibration attenuation in y-direction

Benefiting from the unique lattice coupling effect, the coupled vibration component in the y-direction exhibits a maximum attenuation of − 25.70 dB at 10 kHz and a minimum attenuation of − 14.88 dB at 14.605 kHz, achieving synchronous attenuation with the z-direction. This indicates that the structure not only performs well in the vibration excitation direction but also effectively suppresses coupled vibrations, thereby further enhancing the stability of the system. Compared with traditional multidirectional vibration-damping methods, such as multilayer composite structures or complex mechanical damping systems, this structure not only achieves multidirectional vibration-damping but also features a simpler construction and lower manufacturing costs.

3) Process realization advantages

As a micro-nano-scale phononic crystal, this structure is significantly downsized compared with traditional locally resonant phononic crystals and adopts a planar-topology configuration that is highly compatible with standard MEMS fabrication processes. This not only significantly enhances the manufacturability and integration level of the device but also ingeniously overcomes the two major limitations of traditional non-planar LRPnCs: first, the difficulties in micro-and nano-machining brought about by complex three-dimensional structures; second, the process compatibility issues that arise during multilayer assembly.

In practical applications, by arranging the LRPnC plate around the device in a specific manner, it can directly absorb the vibrational energy transmitted from the substrate, thereby achieving effective vibration isolation and protection for the device. Compared with traditional vibration isolation devices, this method can be directly integrated with the manufacturing of MEMS resonators, eliminating the need for additional assembly steps and significantly enhancing the reliability and stability of the system. The specific arrangement is shown in Fig.10.

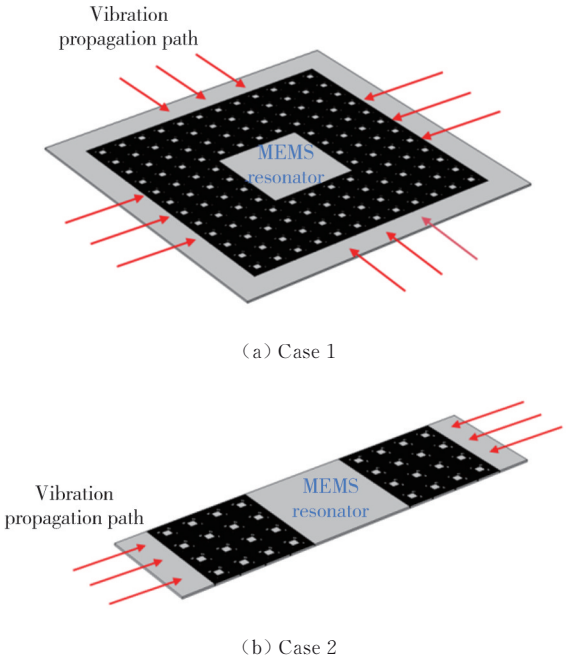

Fig. 10 Vibration isolation applications of LRPnC plate

This LRPnC plate, which combines broadband, multidirectional attenuation characteristics and process compatibility, is particularly suitable for high-precision vibration control in MEMS. Taking a typical MEMS gyroscope as an example, this structure can simultaneously suppress vibrations from the base (z-direction) and the coupling vibrations of the sensitive axis (y-direction), thereby significantly enhancing the vibration resistance of the gyroscope. Therefore, these characteristics provide an innovative solution for the design of high-performance MEMS inertial sensors and are expected to promote the development of related technologies.

3 Conclusions

In this paper, we present a chip-scale lLRPnC plate structure based on a folded helical beam design, aimed at enhancing the vibration resistance of MEMS resonators in complex environments. First, we utilized finite

element simulations to analyze the band structure and vibration modes of the folded helical beam LRPnC, revealing the mechanism of its bandgap formation. We further systematically investigated the influence of different unit cell array layers on the vibration reduction performance and ultimately designed a phononic crystal plate structure with a 4×4 array arrangement. Finite element simulation results indicate that the designed LRPnC plate structure exhibits excellent vibration reduction performance within its bandgap range (9.867—14.605 kHz): it achieves stable attenuation exceeding −30 dB in the z-direction while effectively suppressing y-direction coupling vibrations induced by x-direction propagating waves. Moreover, the phononic crystal features a chip-scale size, and its planar structure is fully compatible with MEMS fabrication processes, overcoming the limitations of traditional phononic crystals in micro- and nano-scale applications and paving a new direction for the development of MEMS vibration isolation.

Acknowledgement

This work was supported by National Natural Science Foundation of China (No.62271262).

Declaration of conflicting interests

The authors have no conflict of interests related to this publication.

References

[1] PLATZ D, SCHMID U. Vibrational modes in MEMS resonators. Journal of Micromechanics and Microengineering. 2019, 29(12): 123001.

[2] LIU Z M, AYAZI F. A review of eigenmode and frequency control in piezoelectric MEMS resonators. IEEE Transactions on Ultrasonics, Ferroelectrics, and Frequency Control, 2023, 70(10): 1172-1188.

[3] ALI RAZA BUKHARI S, SALEEM M M, HAMZA A, et al. A novel design of high resolution MEMS gyroscope using mode-localization in weakly coupled resonators. IEEE Access, 2021, 9: 157597-157608.

[4] CHEN H, YUAN Q, ZHANG Y X, et al. Review of switchable/tunable MEMS resonators. Transducer and Microsystem Technologies, 2025, 44(1): 6-10.

[5] LAN F F. Research on structural design and fabrication process of MEMS piezoelectric resonant pressure sensor. Chongqing: Chongqing University, 2023.

[6] SONG L J, LU M H, ZHAO S H, et al. MEMS inertial shoe-mounted pedestrian navigation system. Flight Control & Detection, 2023, 6(5): 61-68.

[7] THIRUVENKATANATHAN P, YAN J Z, SESHIA A A. Differential amplification of structural perturbations in weakly coupled MEMS resonators. IEEE Transactions on Ultrasonics, Ferroelectrics, and Frequency Control, 2010, 57(3): 690-697.

[8] DONG L X, TAO J P, BAO J Y, et al. Anchor loss variation in MEMS wine-glass mode disk resonators due to fluctuating fabrication process. IEEE Sensors Journal, 2016, 16(18): 6846-6856.

[9] KRUSHYNSKA A O, TORRENT D, ARAGÓN A M, et al. Emerging topics in nanophononics and elastic, acoustic, and mechanical metamaterials: an overview. Nanophotonics, 2023, 12(4): 659-686.

[10] KUSHWAHA M S, HALEVI P, DOBRZYNSKI L, et al. Acoustic band structure of periodic elastic composites. Physical Review Letters, 1993, 71(13): 2022-2025.

[11] LIU Z Y, ZHANG X X, MAO Y W, et al. Locally resonant sonic materials. Science, 2000, 289(5485): 1734-1736.

[12] JIANG W F, YIN G F, XIE L F, et al. Multifunctional 3D lattice metamaterials for vibration mitigation and energy absorption. International Journal of Mechanical Sciences, 2022, 233: 107678.

[13] YAO Z C, ZEGA V, SU Y, et al. Design, fabrication and experimental validation of a metaplate for vibration isolation in MEMS. Journal of Microelectromechanical Systems, 2020, 29(5): 1401-1410.

[14] ZEGA V, GAZZOLA C, BUFFOLI A, et al. A defect-based MEMS phononic crystal slab waveguide//2022 IEEE 35th International Conference on Micro Electro Mechanical Systems Conference, January 9-13, 2022, Tokyo, Japan. New York: IEEE, 2022: 176-179.

[15] CHAI Z M, LIU H C, XIANG J W. Low-frequency broadband vibration reduction based on a square spiral beam local resonance phononic crystal. Japanese Journal of Applied Physics, 2024, 63(3): 034002.

[16] ZHANG L. Band structure and bandgap design of beam-supported binary phononic crystals. Dalian: Dalian University of Technology, 2023.

[17] WANG Y H, ZHANG Z W, CHENG Y, et al. Pseudospin modes of surface acoustic wave and topologically protected sound transmission in phononic crystal. Acta Physica Sinica, 2019, 68(22): 264-271.

[18] JO S H, YOON H J, SHIN Y C, et al. Elastic wave localization and harvesting using double defect modes of a phononic crystal. Journal of Applied Physics, 2020, 127(16): 164901.

[19] JI T. Research on vibration model and isolation effect of locally resonant phononic crystals. Shanghai: Shanghai Jiao Tong University, 2008.

[20] WANG G, SHAO L H, LIU Y Z, et al. Accurate evaluation of lowest band gaps in ternary locally resonant phononic crystals. Chinese Physics, 2006, 15(8): 1843-1848.

[21] JIANG S. Research on low-frequency wide bandgap phononic crystals. Wuhan: Huazhong University of Science

and Technology, 2018.
[22] SHAO T. Study on acoustic wave microfluidic devices based on phononic crystals. Hangzhou: Zhejiang University, 2023.
[23] XIAO Y, WEN J, WEN X. Flexural wave band gaps in locally resonant thin plates with periodically attached spring-mass resonators. Journal of Physics D-Applied Physics, 2021, 45(19): 195401-195412.
[24] WU J H, ZHANG S W, SHEN L. Low-frequency vibration characteristics of periodic spiral resonators in phononic crystal plates. Journal of Mechanical Engineering, 2013, 49(10): 62-69.
[25] YIP K L S, JOHN S. Sound trapping and waveguiding in locally resonant viscoelastic phononic crystals. Scientific Reports, 2023, 13: 15313.
[26] DING X, ZHAO Y, HU N, et al. Experimental and numerical study of nonlinear lamb waves of a low-frequency S_0 mode in plates with quadratic nonlinearity. Materials (Basel), 2018, 11(11): E2096.

MEMS谐振器中用于隔振的折叠螺旋梁声子晶体板设计

李思怡, 徐李疆, 姜　波*

南京理工大学 机械工程学院, 江苏 南京 210094

摘　要： 在复杂环境中增强微机电系统(Micro-electro-mechanical systems, MEMS)谐振器的抗振性能是一个亟待解决的关键问题。为此, 提出了一种基于折叠螺旋梁结构的芯片级局域共振型声子晶体(Locally resonant phononic crystal, LRPnC)板。通过有限元仿真与理论分析, 深入研究了该结构的能带特性与振动抑制机理。研究结果表明, 该结构在9.867－14.605 kHz频率范围内展现出完全带隙特性, 且通过调整结构参数可实现对带隙的有效调控。在此基础上, 进一步研究了晶胞阵列层数对减振性能的影响规律, 并构建了有限周期LRPnC板。数值研究表明, 该LRPnC板在带隙范围内可实现超过－30 dB的振动衰减, 同时有效抑制了x向传播波引发的y向耦合振动。此外, 其芯片级尺寸和平面化结构设计为声子晶体技术在MEMS隔振领域的工程应用提供了新的思路和方法。

关键词： 微机电系统谐振器; 振动隔离; 局域共振型声子晶体; 芯片级声学超材料; 有限元仿真

引用格式： LI Siyi, XU Lijiang, JIANG Bo. Design of phononic crystal plate with folded helical beam for vibration isolation in MEMS resonators. Journal of Measurement Science and Instrumentation, 2025, 16(3): 323-333. DOI: 10.62756/jmsi. 1674-8042.2025031